Cell Reports

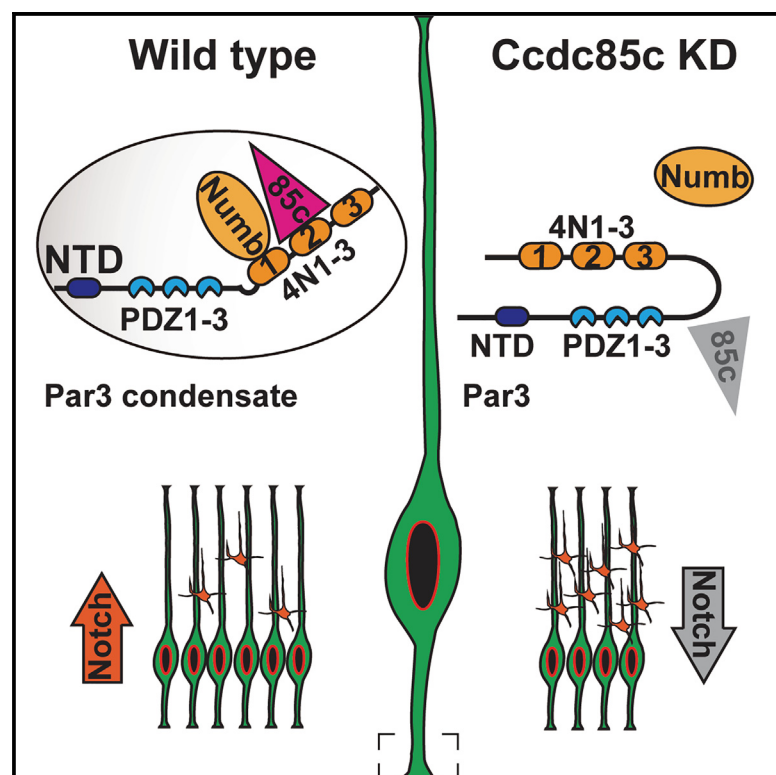# Ccdc85c-Par3 condensates couple cell polarity with Notch to control neural progenitor proliferation

Graphical abstract

Highlights

- Ccdc85c interacts with the polarity protein Par3 to control RGC proliferation

- Downregulation of Ccdc85c leads to RGC differentiation

- Ccdc85c relieves the closed conformation of Par3 to facilitate the recruitment of Numb

- Ccdc85c regulates Notch pathway via phase separation coupled to percolation (PSCP) of Par3

Authors

Jiawen Xu, Xin Deng, Aihong Gu, ...,
Yiqing Zhang, Wenyu Wen, Yunli Xie

Correspondence

wywen@fudan.edu.cn (W.W.),
yunli.xie@fudan.edu.cn (Y.X.)

In brief

Proper control of the balance between proliferation and differentiation of radial glial cells (RGCs) is essential for brain development. Xu et al. show that Ccdc85c, a coiled-coil protein, interacts with the polarity protein Par3 to control RGC proliferation by regulating the Notch signaling pathway via phase separation coupled to percolation (PSCP).

CellPress

Article

Ccdc85c-Par3 condensates couple cell polarity with Notch to control neural progenitor proliferation

Jiawen Xu,[1,3] Xin Deng,[1,3] Aihong Gu,[1,3] Yuqun Cai,[1,3] Yunyun Huang,[1] Wen Zhang,[1] Yiqing Zhang,[1] Wenyu Wen,[1,2,*] and Yunli Xie[1,4,*]

[1]Department of Anesthesia, State Key Laboratory of Medical Neurobiology and MOE Frontiers Center for Brain Science, Institutes of Brain Science, Zhongshan Hospital, Department of Neurosurgery, Huashan Hospital, Institutes of Biomedical Sciences, School of Basic Medical Sciences, Fudan University, Shanghai 200032, China
[2]The Shanghai Key Laboratory of Medical Epigenetics, National Center for Neurological Disorders, Fudan University, Shanghai 200032, China
[3]These authors contributed equally
[4]Lead contact
*Correspondence: wywen@fudan.edu.cn (W.W.), yunli.xie@fudan.edu.cn (Y.X.)
https://doi.org/10.1016/j.celrep.2023.112677

SUMMARY

Polarity proteins regulate the proliferation and differentiation of neural progenitors to generate neurons during brain development through multiple signaling pathways. However, how cell polarity couples the signaling pathways remains unclear. Here, we show that coiled-coil domain-containing protein 85c (Ccdc85c) interacts with the polarity protein Par3 to regulate the proliferation of radial glial cells (RGCs) via phase separation coupled to percolation (PSCP). We find that the interaction with Ccdc85c relieves the intramolecular auto-inhibition of Par3, which leads to PSCP of Par3. Downregulation of Ccdc85c causes RGC differentiation. Importantly, the open conformation of Par3 facilitates the recruitment of the Notch regulator Numb to the Par3 condensates, which might prevent the attenuation of Notch activity to maintain RGC proliferation. Furthermore, ectopic activation of Notch signaling rescues RGC proliferation defects caused by the downregulation of Ccdc85c. These results suggest that Ccdc85c-mediated PSCP of Par3 regulates Notch signaling to control RGC proliferation during brain development.

INTRODUCTION

Tight control of the balance between proliferation and differentiation of neural progenitor cells is essential for generating the proper number of neurons during brain development. In the developing mouse neocortex, radial glial cells (RGCs) are neural progenitor cells that produce most, if not all, cortical neurons directly or indirectly.[1] At the onset of neurogenesis around embryonic day 10.5 (E10.5), RGCs mainly undergo proliferative divisions to expand the progenitor pool. During the peak of neurogenesis around E14.5, RGCs divide asymmetrically to generate either neurons or intermediate progenitors (IPs) that undergo limited rounds of symmetric division to generate neurons.[2–4] RGCs are highly polarized and connect the ventricular zone (VZ) surface with apical processes and the pial surface with basal processes, while their cell bodies are located in the VZ adjacent to the ventricle.[5] After differentiation, nascent neurons migrate radially from the VZ along the basal processes of RGCs into the cortical plate.[6] During brain development, early-born neurons settle in the deep layers, and late-born neurons populate the superficial layers, which results in an "inside-out" cortical pattern.[7] Disruption of the balance between proliferation

and differentiation of RGCs leads to abnormal neuronal production, which ultimately results in cortical malformation.[8,9]

The polarized structure of RGCs has been implicated in the control of their proliferation and differentiation.[4] Particularly, the preferential inheritance of apical or basal processes by the daughter cells after RGC divisions has instructive roles in determining the daughter cell fate.[10–12] One of the underlying mechanisms is that certain molecular determinants are asymmetrically segregated into daughter cells, for example, the RNA-binding protein Staufen2[13,14] and the polarity protein partition defective protein 3 (Par3).[15,16] However, how these proteins regulate RGC proliferation and differentiation remains poorly understood. In *Drosophila* neuroblasts, the polarity protein Bazooka (Par3 homolog in *Drosophila*) interacts with other polarity proteins, such as Par6 and atypical protein kinase C (aPKC), to form a core complex and asymmetrically localizes at the apical cortex of neuroblasts during mitosis of the cell cycle,[17,18] which is essential for the subsequent asymmetric segregation of cell fate determinates.[17] In the mammalian brain, Par3 is located in the adherens junctions at the VZ surface[19] and asymmetrically segregates into the daughter cell with the RGC fate through the interaction with Notch signaling.[16] Loss of Par3 leads to RGC
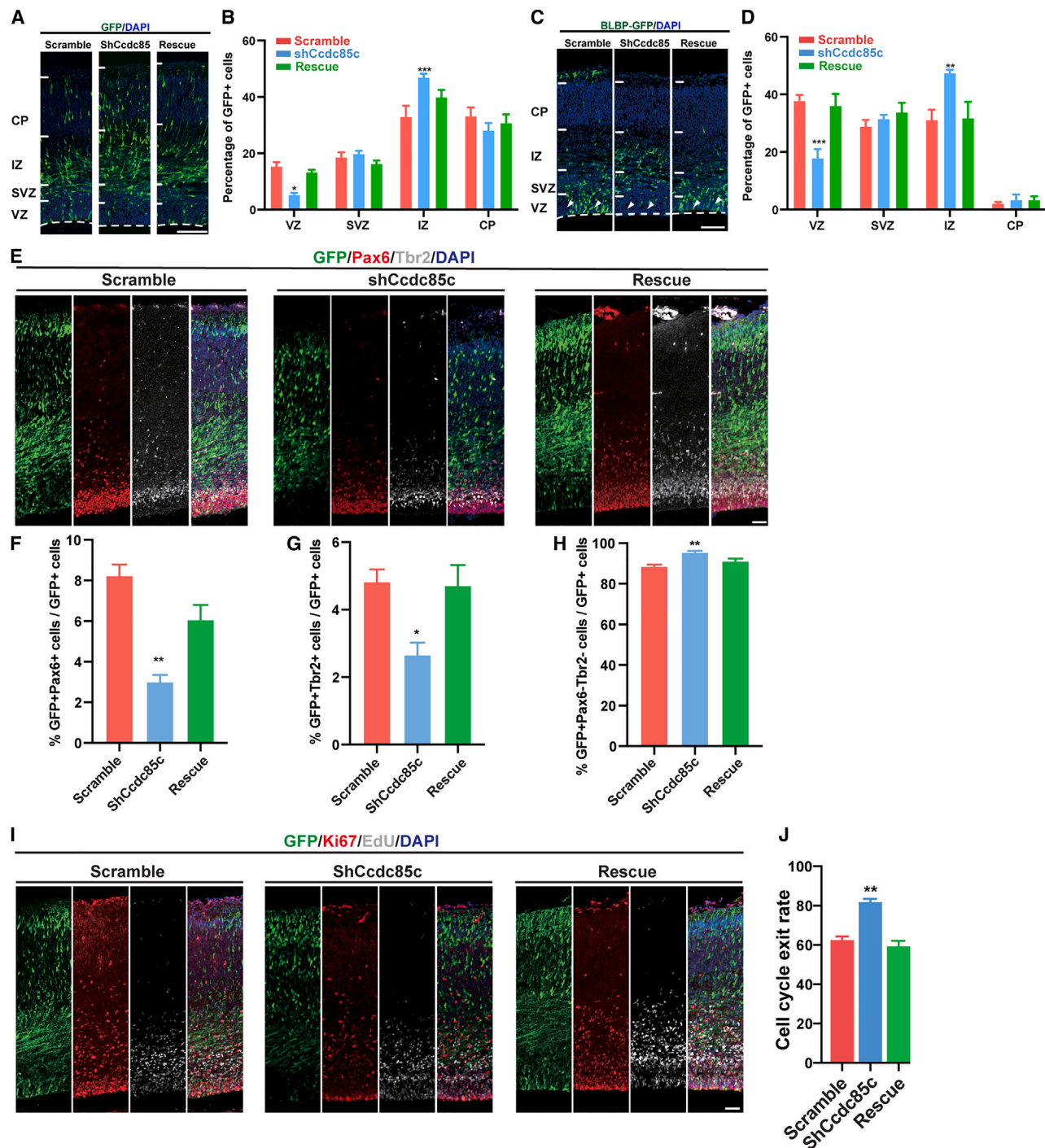
Figure 1. Downregulation of Ccdc85c leads to the delamination of RGCs from the apical surface

(A) Representative images of brain sections electroporated with plasmids expressing scramble, ShCcdc85c, or ShCcdc85c together with a shRNA-resistant form of human CCDC85C (hCCDC85C; rescue is used to represent this group in the following text). The apical surface is outlined with a dashed line.

(B) The quantification of the distribution of Ccdc85c downregulated progenitors (GFP$^+$ cells) shown in (A).

(C) Representative images of brain sections electroporated with plasmids expressing GFP with BLBP promoter (BLBP-GFP) together with plasmids expressing scramble, ShCcdc85c, or ShCcdc85c and hCCDC85C (rescue).

(D) The quantification of the distribution of GFP$^+$ cells shown in (C). At least 3 brains were used for analysis in each condition.

(E) Representative images of sections stained for Pax6, Tbr2 in scramble, ShCcdc85c, or rescue construct electroporated brains. Embryonic brains were electroporated at E14.5 and analyzed 3 days later.

(legend continued on next page)

differentiation.[15,16] However, the detailed mechanisms of Par3-mediated RGC proliferation remain elusive.

To address how polarity cues regulate RGC development, we searched for the interaction partners of the polarity protein Par3 and identified the coiled-coil domain-containing protein 85c (Ccdc85c) as an interaction partner. Ccdc85c is localized at the apical junctions of RGCs in the developing mouse neocortex.[20] Disruptions of Ccdc85c have been implicated in hemorrhagic hydrocephalus.[20,21] However, the exact roles of Ccdc85c in brain development have not been addressed. Here, we found that the interaction between Par3 and Ccdc85c is essential for the maintenance of RGC proliferation through Par3-mediated phase separation.

RESULTS

Loss of Ccdc85c leads to RGC differentiation

To examine the role of Ccdc85c in RGCs, we first generated a short hairpin RNA (shRNA) against Ccdc85c (ShCcdc85c) to interfere with Ccdc85c expression (Figure S1). The attenuation of Ccdc85c was rescued by over-expression of an RNAi-resistant form of human CCDC85C (hCCDC85C) (Figure S1). To study whether Ccdc85c regulates RGC development, we electroporated plasmids expressing ShCcdc85c into cortical progenitor cells of the mouse embryonic brains through *in utero* electroporation at E14.5. When analyzing the brains 3 days after electroporation at E17.5, we found that the distribution of electroporated cells was altered upon downregulation of Ccdc85c (Figure 1A). In brains electroporated with plasmids expressing scramble, RGCs were distributed in the VZ, and neurons migrated away from the VZ to the cortical plate (CP) (Figure 1A). However, we observed few cells in the VZ when Ccdc85c was downregulated (Figure 1A), while most cells expressing ShCcdc85c were distributed in the intermediated zone (IZ) (Figures 1A and 1B). The abnormal distribution of ShCcdc85c electroporated cells was attenuated by the over-expression of hCCDC85C (Figures 1A and 1B). When we examined the neuronal distribution at postnatal day 7 (P7), when neuronal migration is completed, we found that neurons lacking the expression of Ccdc85c could not migrate properly (Figure S2). To further confirm the reduction of RGCs in the VZ, we co-electroporated constructs expressing ShCcdc85c and constructs expressing GFP driven by a BLBP promoter (BLBP-GFP), which specifically is expressed in RGCs and differentiating progenitors.[22] We found that GFP+ RGCs were largely absent in the VZ (Figures 1C and 1D) of ShCcdc85c electroporated brains, suggesting that RGCs may undergo differentiation upon the downregulation of Ccdc85c.

To ask whether the reduction of RGCs in the VZ was due to the differentiation of RGCs upon the loss of Ccdc85c, we examined the cell fate of RGCs. We found that the number of Pax6-expressing neural progenitors (Pax6+ progenitors) was reduced when Ccdc85c was knocked down compared with the scramble electroporated progenitors (Figures 1E and 1F), which could be recused by over-expression of hCCDC85C (Figures 1E and 1F). RGCs can differentiate into IPs, which also contribute to neuronal production. We then asked whether the number of IPs was altered when Ccdc85c was attenuated. Indeed, we found that the number of IPs was reduced in ShCcdc85c electroporated progenitors by examining the number of cells expressing Tbr2, a marker for IPs, suggesting that Ccdc85c is essential for the maintenance of the progenitor pool (Figures 1E and 1G). The reduction of the progenitor pool could be caused by an increase in neuronal differentiation. To overcome the difficulties in identifying neuronal identity using the traditional immature neuronal marker Tuj1, we examined the number of cells that were negative for both Pax6 and Tbr2, as no glial cells are generated at this time. We found that the number of neurons (GFP+, Pax6−, Tbr2−) was increased (Figures 1E and 1H). To further confirm this, we performed a cell cycle exit assay, which examines the number of cells exiting the cell cycle by labeling cells with EdU and Ki67 (Figure 1I). We performed electroporation at E14.5 with constructs expressing either only ShCcdc85c or ShCcdc85c paired with hCCDC85C (rescue). EdU was administrated at E16.5, and the embryonic brains were analyzed 24 h later. When examining the number of cells that exited the cell cycle (percentage of GFP+EdU+ Ki67− cells in total GFP+EdU+ cells), we found a significant increase in the cell cycle exit rate when Ccdc85c was downregulated, which could be rescued by expressing hCCDC85C (Figures 1I and 1J). Taken together, these data demonstrate that Ccdc85c is essential for the maintenance of neural progenitor proliferation.

Par3 interacts with Ccdc85c through the 4N2 domain

The phenotype resulting from the loss of Ccdc85c is similar to the phenotype resulting from the lack of the polarity protein Par3 in RGCs during brain development.[15,16] We then examined the expression pattern of Par3 and Ccdc85 in RGCs. To overcome the lack of high-quality antibodies for immunostaining of both Par3 and Ccdc85c, we performed the electroporation with plasmids expressing Par3 and Ccdc85c in RGCs. We found that Ccdc85c is co-localized with Par3 at the endfeet of RGCs (Figure S3A). Interestingly, consistent with the asymmetric distribution of Par3 during RGC divisions,[16] we found that Ccdc85c localized at the apical endfeet of RGCs in the interphase (Figure S3B) and showed an asymmetric distribution pattern together with Par3 during mitosis (7 cells out of 13 cells examined) (Figure S3B). These data suggest that Ccdc85c may interact with Par3 to regulate RGC proliferation.

We confirmed the interaction between Par3 and Ccdc85c by performing a co-immunoprecipitation experiment (Figure 2A).

(F–H) Quantifications of Pax6-expressing progenitors (F), Tbr2+ intermediate progenitors (G), and neurons that are Pax6− and Tbr2− (H).

(I) Representative images of sections stained for Ki67 and EdU examining the cell cycle exit rate in scramble, ShCcdc85c or rescue construct electroporated brains.

(J) Quantification of the number of progenitors that exited the cell cycle that is positive for GFP and EdU but negative for Ki67. VZ, ventricular zone; SVZ, subventricular zone; IZ, intermediate zone; CP, cortical plate.

Scale bar: 50 μm. At least three brains were analyzed for each condition. Data are shown as mean ± SEM. One-way analysis of variance (ANOVA) test was used. *p < 0.05, **p < 0.01.
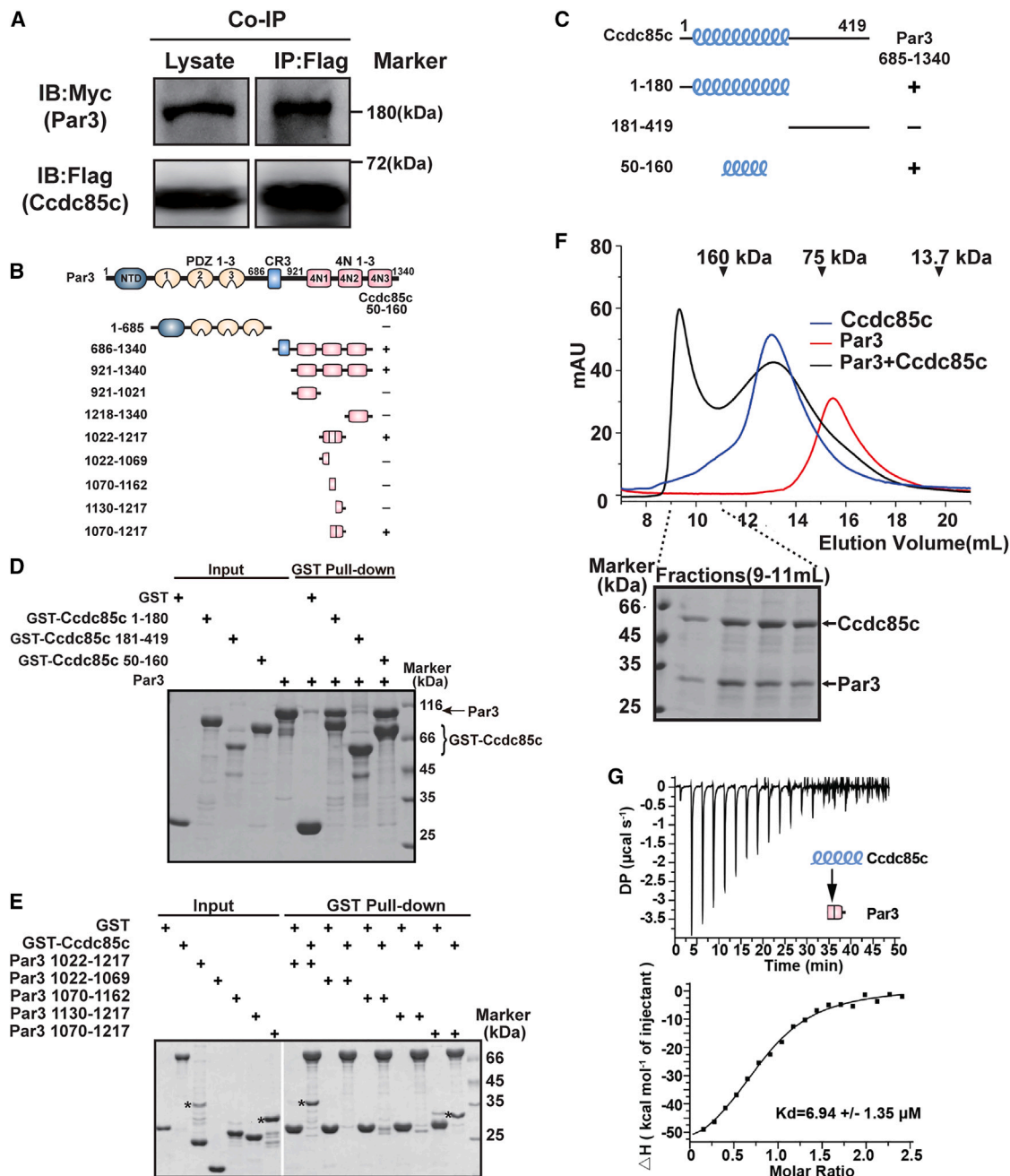
Figure 2. Ccdc85c coiled-coil domain specifically binds to the 4N2 region of Par3

(A) Co-immunoprecipitation (coIP) confirms the interaction between Myc-Par3 and FLAG-Ccdc85c.

(B) Schematic diagrams showing the domain organizations of Par3. A summary of the binding properties of various Par3 fragments to Ccdc85c (50–160), as shown in (E), is given at the right of the panel.

(C) Schematic diagrams showing the domain organizations of Ccdc85c. A summary of the binding properties of various Ccdc85c fragments to Par3C (aa 686–1340), as shown in (D), is given at the right of the panel.

(D) GST pull-down assay of Trx-Par3C with MBP-His-GST-tagged hCcdc85c (1–180, 50–160) and GST-tagged hCcdc85c fragments (181–419).

(E) GST pull-down assay of various Trx-tagged human Par3 fragments with MBP-His-Ccdc85c (50–160).

(F) Analytical gel filtration analysis showing that Trx-Par3 (1070–1217) forms a stable complex with MBP-His-Ccdc85c (50–160). The elution volumes of the molecular size markers are indicated at the top of the panel.

(G) ITC-based measurement of the binding between Trx-Par3 (1070–1217) and MBP-His-Ccdc85c (50–160).
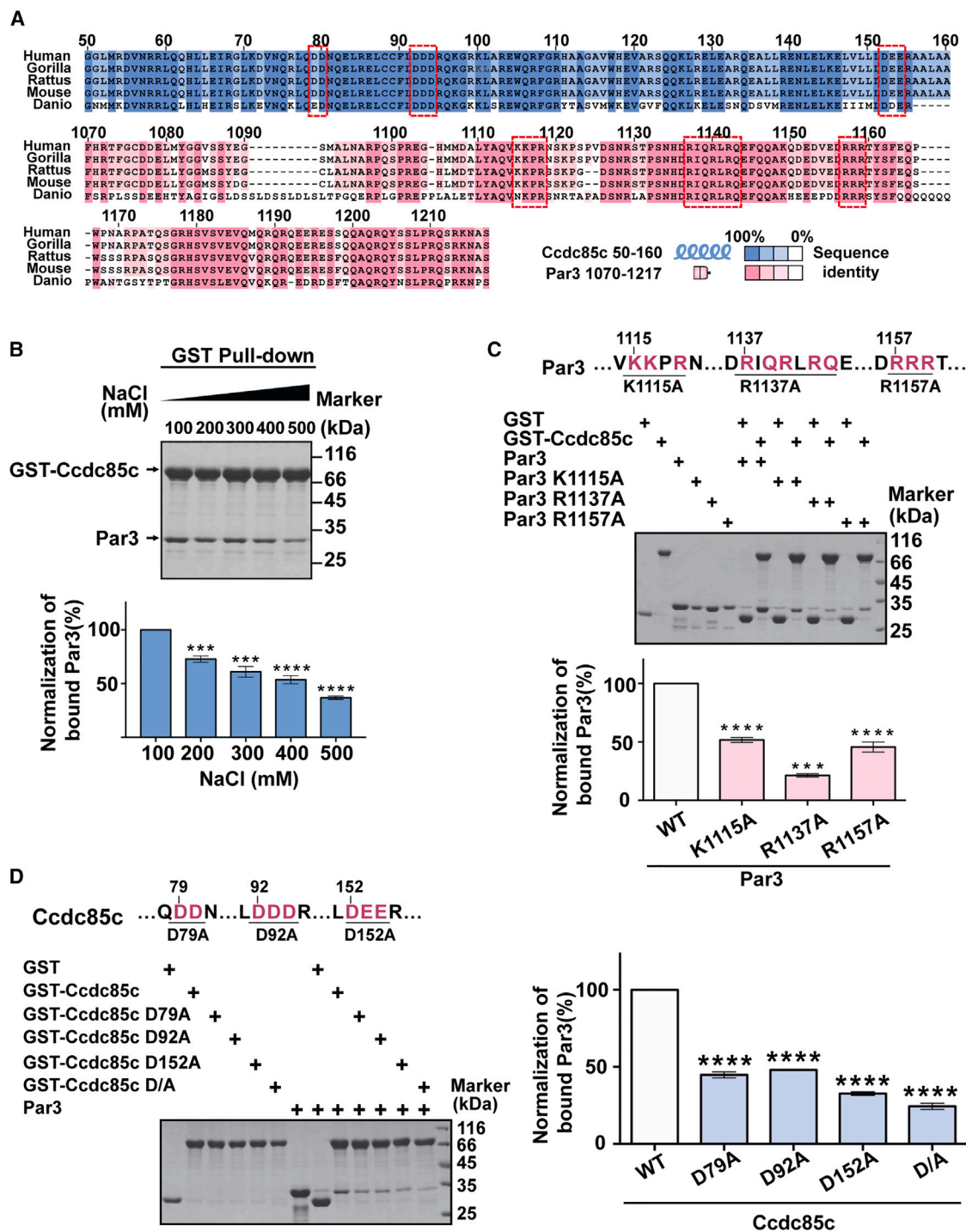
Figure 3. Ccdc85c binds to Par3 via the electrostatic interaction

(A) Multiple sequence alignment of Ccdc85c and Par3 in different species and color coded by sequence identity in blue or pink, respectively. The residues responsible for electrostatic interaction are indicated with red rectangles.

(B) GST pull-down assay showing that NaCl significantly weakens the interaction between MBP-His-Ccdc85c (50–160) and Trx-Par3 (1070–1217) in a dose-dependent manner.

(C) Mutagenesis of the positively charged clusters in Trx-Par3 (1070–1217) impairs the binding to MBP-His-Ccdc85c (50–160). K$^{1115–1116}$R^{1118}/A is referred to as K1115A, R^{1137}Q^{1139}R^{1140}R^{1142}Q^{1143}/A as R1137A, and R$^{1157–1159}$/A as R1157A.

(legend continued on next page)

Par3 contains an N-terminal domain (NTD) followed by three PDZ domains at the N terminus (referred to as Par3N hereafter) and three 4N domains at the C terminus (referred to as Par3C) (Figure 2B),[23,24] and Ccdc85c contains a coiled-coil domain at the N terminus (Figure 2C). GST pull-down experiments showed that the coiled-coil domain (aa 50–160) of Ccdc85c directly interacted with Par3 (Figures 2C and 2D). Though PDZ domains are essential protein-binding modules,[25] we found that the C-terminal part of the Par3 4N2 domain (aa 1070–1217) was responsible for binding to Ccdc85c (Figures 2B and 2E). In line with the pull-down results, analytical gel filtration analysis and isothermal titration calorimetry (ITC) measurement demonstrated that Par3 (1070–1217) formed a stable complex with Ccdc85c (50–160), with a dissociation constant at about 7 μM (6.94 ± 1.35 μM) (Figures 2F and 2G). Taken together, we identified Ccdc85c as a binding partner of Par3.

Identification of Par3-Ccdc85c binding sites

We next investigated how Ccdc85c interacts with Par3. Ccdc85c and Par3 are highly conserved among the vertebrates (Figure 3A). Sequence analysis of Par3 and Ccdc85c revealed several evolutionarily conserved clusters of charged amino acids (highlighted with red rectangles, Figure 3A). Intriguingly, a high salt concentration (up to 500 mM) significantly reduced the amount of Par3 pulled down by Ccdc85c (Figure 3B), suggesting a charge-mediated interaction between Par3 and Ccdc85c. We then substituted these charged residues to alanine to probe their influence on Ccdc85c/Par3 binding. The $K^{1115-1116}R^{1118}$/A (referred to as K1115A hereafter), $R^{1137}Q^{1139}R^{1140}R^{1142}Q^{1143}$/A (referred to as R1137A hereafter), and $R^{1157-1159}$/A (referred to as R1157A hereafter) mutants of Par3 all showed a weakened binding avidity to Ccdc85c (Figure 3C). Furthermore, mutations of D^{79-80}/A (referred to as D79A hereafter), D^{92-94}/A (referred to as D92A hereafter), and $D^{152}E^{153-154}$/A (referred to as D152A hereafter) of Ccdc85c significantly attenuated the interaction with Par3, and a combinational mutation of the negatively charged residues (referred to as D/A hereafter) above disrupted Ccdc85c/Par3 packing (Figure 3D). Taken together, our biochemical analysis indicated that the specific interaction between Par3 and Ccdc85c is mainly driven by charge-charge interactions.

The interaction between Ccdc85c and Par3 is required for the maintenance of RGCs in the VZ

To ask whether the interaction between Ccdc85c and Par3 is required for the maintenance of RGCs in the VZ, we performed *in utero* electroporation using constructs expressing ShCcdc85c together with either hCCDC85C or hCCDC85C bearing the D/A mutation (hCCDC85C-D/A) (Figure 3D), which dramatically impaired the interaction between Ccdc85c and Par3 (Figure 4A). Meanwhile, we electroporated plasmids expressing BLBP-GFP for labeling RGCs. While we found that the expression of

hCCDC85C rescued RGC differentiation caused by downregulation of Ccdc85c (Figures 4A–4C), the expression of hCCDC85C harboring the Par3-binding-deficient mutation did not result in rescue phenotype (Figures 4A–4C). In addition, we found that the number of Pax6+ RGCs was reduced upon the interference by ShCcdc85c, which was rescued by the expression of hCCDC85C but not hCCDC85C-D/A (Figures 4A and 4D). These results suggest that the interaction between Ccdc85c and Par3 is important for the maintenance of RGCs in the VZ.

Ccdc85c relieves intramolecular auto-inhibition of Par3 to promote Numb recruitment

We then investigated the mechanism underlying the interaction between Ccdc85c and Par3 in regulating RGC proliferation. Previously, we showed that Par3 exhibits cell cycle-dependent apical condensation through phase separation during *Drosophila* neuroblast asymmetric divisions, thus setting up the apical-basal polarity of neuroblasts at mitosis.[26] To further examine the mechanism of Par3 phase separation, we characterized the saturation concentration (Csat; ~4 μM; Figure S4A) of recombinant Par3N using a spin-down-based absorbance assay.[27] Above this threshold concentration, Par3N concentration in the supernatant reached a plateau, which is the prominent indication of macromolecular phase separation.[28] Consistent with this data, fluorescent microscopy-based measurements showed that condensate formation of iFluor488-labeled Par3N was only observed at or above Csat ~4 μM (Figure S4B). Moreover, the dynamic light scattering (DLS) analysis of Par3N subsaturated solutions suggested the presence of a heterogeneous distribution of clusters (Figure S4C). The average sizes of these clusters shifted toward larger ones as protein concentrations increased and approached Csat, indicating a phase separation coupled to percolation (PSCP).[28] In contrast to pure phase separation, PSCP generates unique distributions of clusters that are specific to the sequence, chemistry, and structure. These clusters can form at concentrations significantly lower than that required for phase separation.[27,29] Given that the PB1 domain has been shown to facilitate condensate formation,[30] it is presumable that the presence of PB1 containing Par6 could further enhance the phase separation of Par3.[26]

Due to the conserved apical localization of Par3 in *Drosophila* and mouse neural stem cells, we asked whether Ccdc85c binding plays a regulatory role in Par3 PSCP. Expression of the full-length GFP-Par3 or mCherry-Ccdc85c (50–160) alone showed a diffused localization pattern in COS7 cells (Figure 5A). Surprisingly, when Par3 was co-expressed with Ccdc85c (50–160), or the full-length Ccdc85c, GFP-Par3 and mCherry-Ccdc85c spontaneously assembled into highly condensed puncta in the cytoplasm, indicating that Ccdc85c binding promotes Par3 PSCP (Figure 5A). In fact, we did observe that Par3 and Ccdc85c assembled into puncta-like structures in RGCs when plasmids expressing Par3 and Ccdc85c were electroporated into

---

(D) Mutagenesis of the negatively charged clusters in MBP-His-Ccdc85c (50–160) impairs the binding to Trx-Par3 (1070–1217). D^{79-80}/A is referred to as D79A, D^{92-94}/A as D92A, and $D^{152}E^{153-154}$/A as D152A, and the combinational mutation of all the above negatively charged residues is referred to as D/A. All statistical data in this figure represent the results of three independent batches of experiments and are expressed as the means ± SD; *p < 0.05, **p < 0.01, ***p < 0.001, and ****p < 0.0001 using one-way ANOVA with Tukey's multiple comparison test.
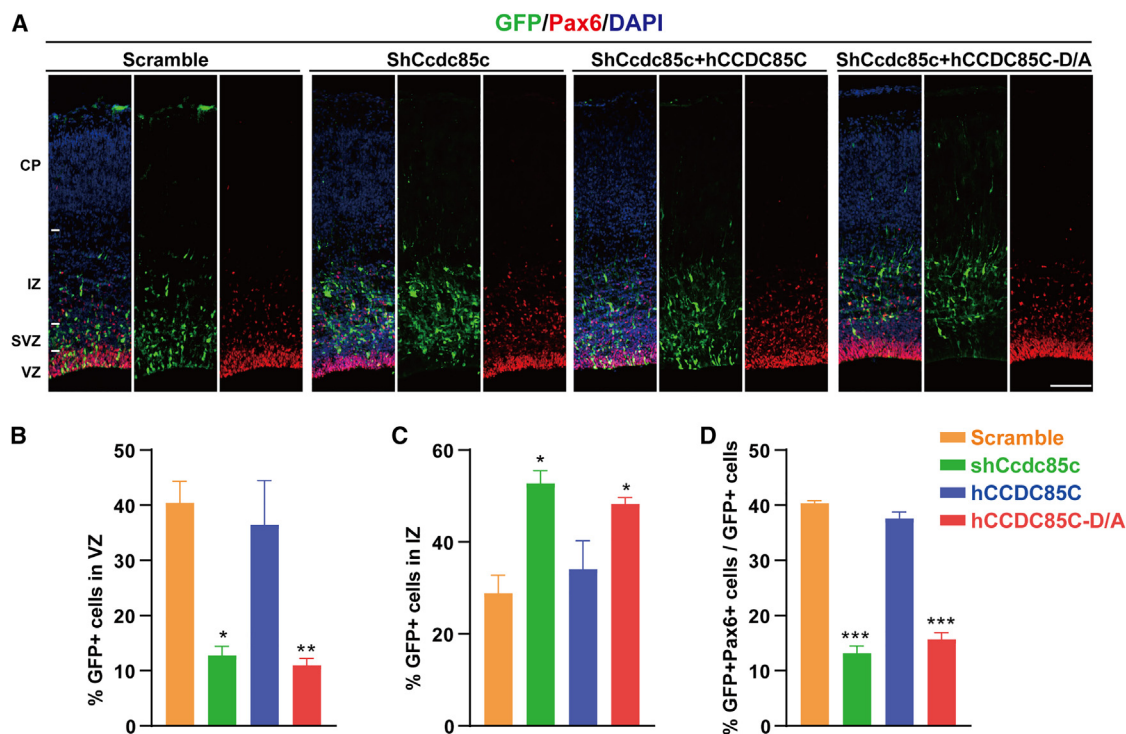
Figure 4. The interaction between Ccdc85c and Par3 is required for the maintenance of RGC in the VZ

(A) Representative images of brain sections electroporated with plasmids expressing BLBP-GFP together with either plasmid expressing scramble, ShCcdc85c, ShCcdc85c and hCCDC85C, or ShCcdc85c and hCCDC85C-D/A. Expression of hCCDC85C-D/A-carrying mutations disrupted the interaction between Ccdc85c and Par3, which could not rescue the delamination of RGC from the VZ, causing the downregulation of Ccdc85c. The identity of the RGC is verified by staining for Pax6.

(B and C) Quantifications of the distribution of GFP+ cells in VZ (B) and IZ (C).

(D) Quantifications of the percentage of GFP+ and Pax6+ cells.

Scale bar: 50 μm. At least three brains were analyzed. Data are shown as mean ± SEM. One-way ANOVA test was used. $*p < 0.05$, $**p < 0.01$, $***p < 0.001$.

RGCs (36% of electroporated cells showed puncta staining) (Figure S3A, arrowheads). This puncta distribution propensity dramatically decreased when the Ccdc85c-binding-deficient Par3R1137A mutant was co-expressed with Ccdc85c (Figures 5A and 5B), suggesting that the interaction between Par3 and Ccdc85c is essential to mediate Par3 PSCP.

A previous study showed that the C-terminal 4N region of Par3 interacts with its N-terminal PDZ domains to induce a closed conformation.[31] We recently showed that the 4N1 and 4N2 regions also inhibit the PSCP ability of Par3.[26] We reasoned that the occurrence of PSCP in Figure 5A might reflect the relief of the auto-inhibited conformation of Par3 upon Ccdc85c binding. To verify our assumption, we first demonstrated that the PDZ1 domain (but not the NTD) in Par3N is responsible for interacting with Par3C via cell lysate GST pull-down assay (Figure S5A). Interestingly, the binding between Par3C and PDZ1 was disrupted when cells were treated with high-concentration salt (1 M NaCl; Figure 5C), suggesting that charge-charge interaction is the main driving force for auto-inhibition of Par3. As Ccdc85c also interacted with the 4N2 region of Par3C via electrostatic interaction (Figure 3), Ccdc85c might compete with Par3 PDZ1 directly for binding to Par3C. Indeed, Ccdc85c significantly impaired the interaction between Par3 PDZ1 and Par3C in a

dose-dependent manner (Figure 5C). However, the Ccdc85c-binding-deficient Par3C R1137A mutant exhibited a similar binding avidity to Par3N compared with Par3C wild type (WT) (Figure S5A), indicating that the PDZ1 and Ccdc85c binding sites on Par3C are only partially overlapped. Taken together, these data suggest that the auto-inhibition of Par3 mediated by PDZ1 and Par3C interferes with the phase separation of the NTD, whereas Ccdc85c binding to Par3C releases PDZ1, leading to NTD-mediated PSCP of Par3.

To further support this model, we fused Cerulean (a cyan fluorescence protein [CFP] variant) and yellow fluorescence protein (YFP) to the N terminus and C terminus of Par3, respectively, and then performed fluorescence resonance energy transfer (FRET) experiments in COS7 cells. Upon bleaching the acceptor fluorophore YFP, the fluorescence intensity of the donor fluorophore Cerulean was markedly increased (Figures 5D and S5B), implying that FRET occurred between the two fluorophores and that the N- and C termini of Par3 were in spatial proximity. When Ccdc85c was co-expressed with CFP-Par3-YFP, the FRET signal was barely detectable (Figures 5D and S5B), indicating that the auto-inhibited conformation of Par3 was relieved and that the two termini were far away from each other. Deletion of 4N1-2, which disrupted the intramolecular interaction,
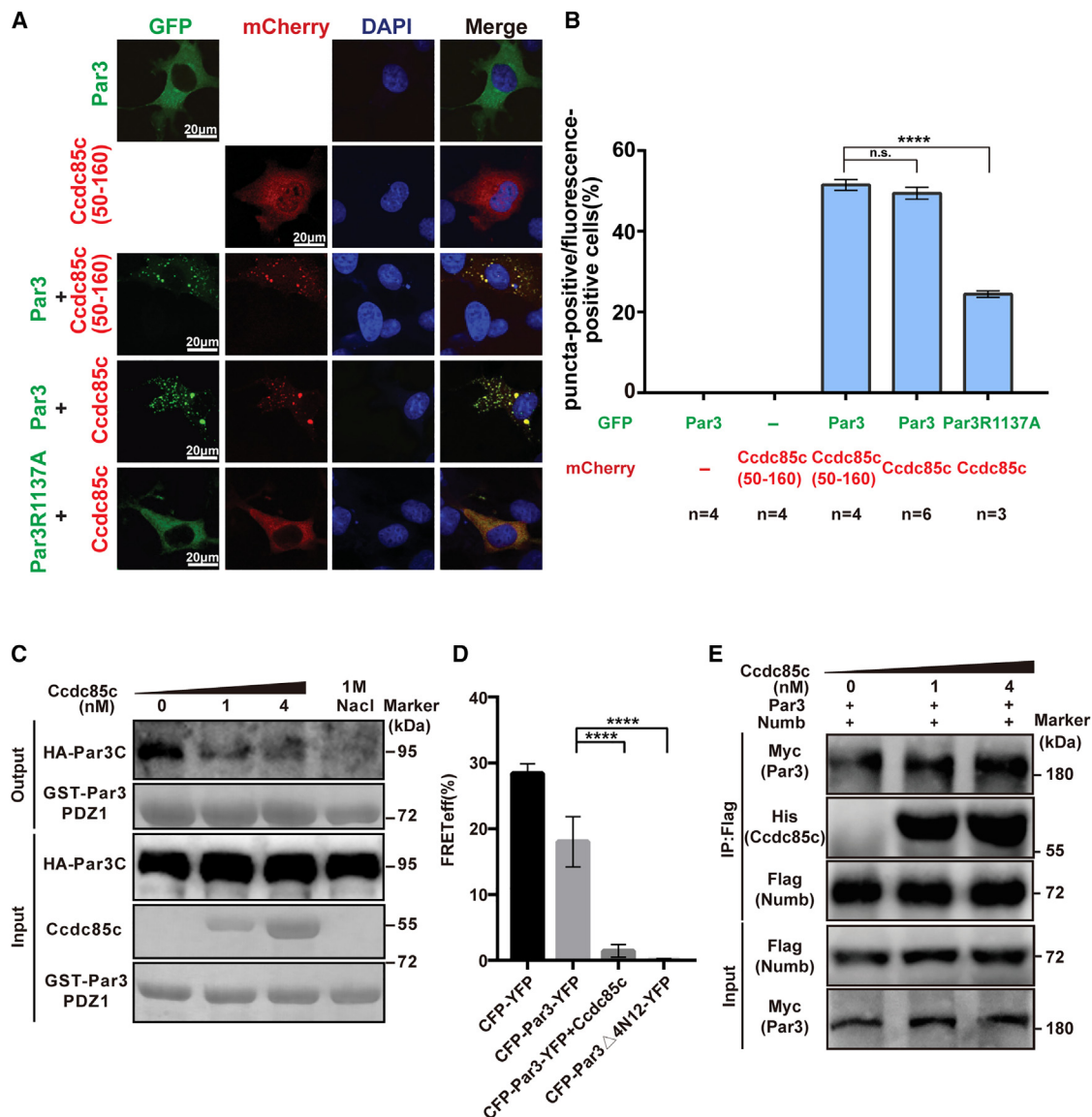
Figure 5. Ccdc85c binding relieves Par3 from the auto-inhibited conformation to undergo phase separation and bind to Numb

(A and B) Par3/Ccdc85c complex forms condensed puncta in living cells.

(A) Representative images showing subcellular localization of Par3 and Ccdc85c, when expressed in COS7 cells. When expressed alone, mCherry-Ccdc85c (50–160) and GFP-Par3 both showed diffused cytoplasmic localization. Co-expression of Ccdc85c and Par3 WT, but not the R1137A mutant, formed scattered bright puncta in cells. Nuclei were stained by DAPI. Scale bar: 20 μm.

(B) Statistical data for (A). n represents the number of independent experimental cell culture batches, with >600 cells counted for each batch. Specimens' statistics are presented as mean ± SEM; n.s., not significant, *p < 0.05, **p < 0.01, and ***p < 0.001 using one-way ANOVA with Tukey's multiple comparison test.

(C) Competition assay showing that MBP-His-Ccdc85c (50–160) could weaken the interaction between GST-Par3 PDZ1 and HA-Par3C in a dose-dependent manner. High-concentration salt (1 M NaCl) could also disrupt PDZ1/Par3C packing. HA-Par3 was detected by western blotting, and the other proteins were stained by Coomassie brilliant blue.

(D) Quantification of FRET efficiency for CFP-YFP (n = 11), CFP-Par3-YFP (n = 11), CFP-Par3-YFP co-expressed with Ccdc85c (n = 11), and CFP-Par3Δ4N1/N2-YFP (n = 11). Error bars represent SEM. ****p < 0.0001.

(E) coIP assay showing that MBP-His-Ccdc85c (50–160) can enhance the interaction between full-length FLAG-Numb and Myc-Par3 in a dose-dependent manner. MBP-His-Ccdc85c (50–160) was stained by Coomassie brilliant blue, and the other proteins were detected by western blotting.

eliminated FRET of CFP-Par3-YFP, serving as the negative control. In line with these data, obvious puncta, which are a signature of phase separation, were only observed for the CFP-Par3-YFP co-expressed with Ccdc85c, or with 4N1-2 truncated, but not for Par3 alone (Figure S5C). Furthermore, we found that the presence of Ccdc85c significantly promoted the interaction between
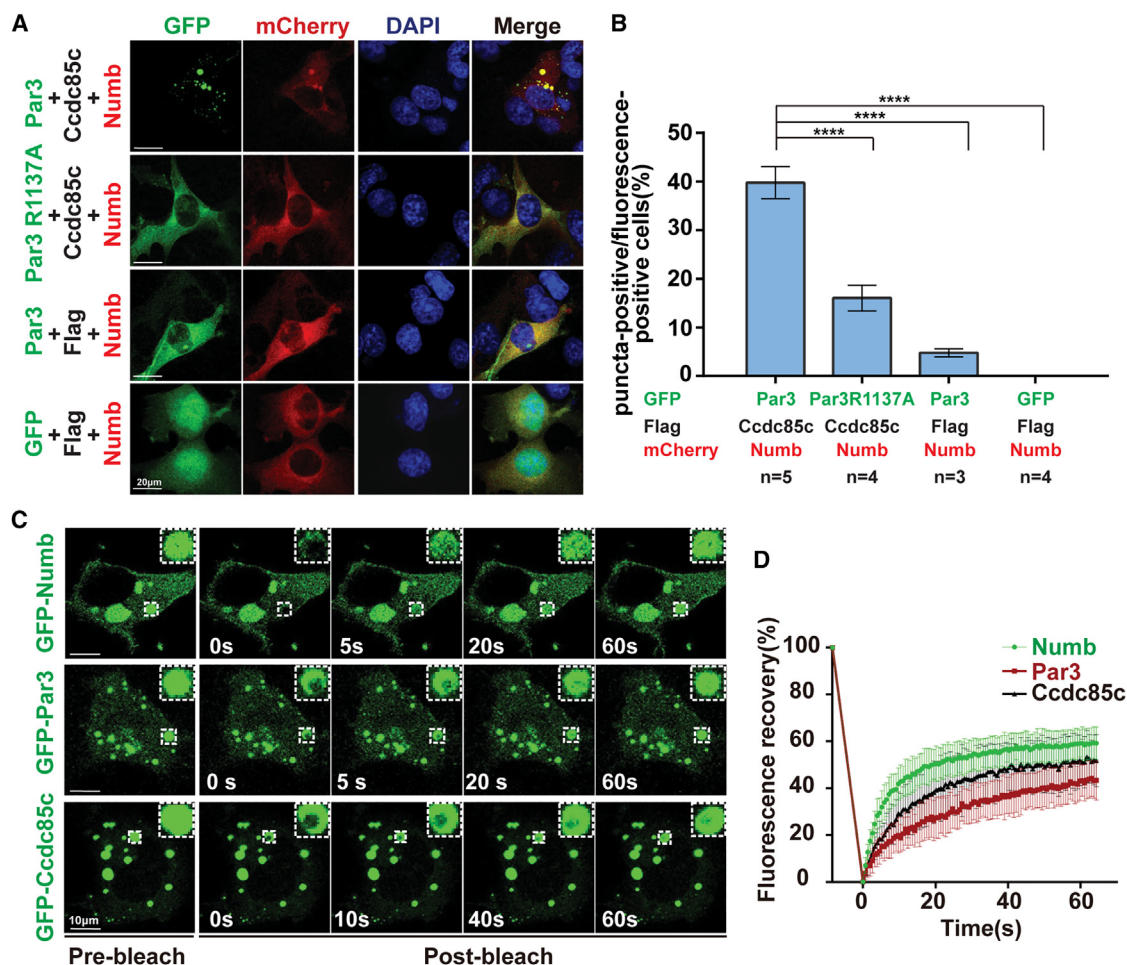
Figure 6. Ccdc85c promotes the recruitment and concentration of Numb to Par3 condensates

(A) Co-expression of mCherry-Numb, GFP-Par3 WT, or R1137A mutant and FLAG-Ccdc85c in COS7 cells. Numb was enriched in Par3 puncta when co-expressed with Ccdc85c, whereas the introduction of the Par3 R1137A mutation or the absence of Ccdc85c led to diffused localization of Numb and Par3 in the cytoplasm. Scale bar: 20 μm.

(B) Statistical data for (A). n represents the number of independent experimental cell culture batches, with >600 cells counted for each batch. Specimens' statistics are presented as mean ± SEM; n.s., not significant, *p < 0.05, **p < 0.01, and ***p < 0.001 using one-way ANOVA with Tukey's multiple comparison test.

(C) Representative time-lapse FRAP images showing that GFP-Numb, GFP-Par3, and GFP-Ccdc85c signals within the condensed puncta recovered within a few minutes after photobleaching. Scale bar: 10 μm.

(D) Statistical data for (C). The green curve represents the averaged FRAP data of 20 puncta from 10 cells. The black curve represents the averaged FRAP data of 15 puncta from 8 cells. The red curve represents the averaged FRAP data of 20 puncta from 14 cells. Time 0 refers to the time point of the photobleaching pulse. All data are represented as mean ± SD.

Par3 and Numb (Figure 5E), an important Par3-interacting partner to regulate Notch signaling.[16] Importantly, the enhanced binding of Par3 with Numb was not due to the interaction between Ccdc85c and Numb (Figure S5D). Taken together, these data demonstrate that the interaction between Ccdc85c and Par3 releases the auto-inhibition to promote PSCP of Par3 and recruitment of its targets (e.g., Numb).

Like Par3 and Ccdc85c, Numb also localizes to adherens junctions of RGCs at the VZ surface and is required for the maintenance of RGC polarity.[32] We wondered whether the junctional localization of Numb relies on Ccdc85c-mediated Par3 local condensation. To test this hypothesis, we co-expressed mCherry-Numb, GFP-Par3, and FLAG-Ccdc85c in COS7 cells

and found that Numb could be effectively recruited into the condensed Par3 puncta as expected (Figures 6A and 6B). Consistently, Par3 was co-localized with Numb in puncta when plasmids expressing Par3 and Numb were electroporated into RGCs (Figure S6). In sharp contrast, the puncta formation disappeared when Par3 harbored the Ccdc85c-binding-deficient R1137A mutation or when Ccdc85c was replaced by a mock vector (Figures 6A and 6B). As a control, mCherry-Numb alone exhibited a diffused distribution in the cytoplasm of COS7 cells (Figure 6A). Importantly, we found that Par3, Ccdc85c, and Numb in the condensed puncta rapidly exchanged with proteins in the surrounding environment, revealed by fluorescence recovery after photobleaching (FRAP) analysis (Figures 6C and 6D),

suggesting the dynamic nature of the condensed puncta. In summary, these data demonstrate that Ccdc85c acts as an important switch to initiate PSCP of Par3, thus leading to the recruitment and concentration of target Numb to Par3 condensates.

Ccdc85c regulates neural progenitor proliferation through Notch signaling

Numb has been reported as an essential Notch regulator.[33–35] Thus, the recruitment and release of Numb to and from the Par3 condensates mediated by the interaction with Ccdc85c could be a regulatory mechanism for Notch activity. Thus, we reasoned that the enhanced neural progenitor differentiation upon the downregulation of Ccdc85c could be rescued by the activation of Notch signaling. To test this hypothesis, we examined whether the activation of Notch activity through the expression of Notch intracellular domain (NICD) could attenuate the differentiation of RGCs from the proliferative VZ upon the downregulation of Ccdc85c. Progenitors were labeled by the plasmids expressing GFP driven by the BLBP promoter (Figure 7). The differentiation of RGCs from the ShCcdc85c brains was rescued by the expression of NICD or the downregulation of Numb and Numb-like (Numbl) (Figures 7A and 7B). To examine the proliferation status of RGCs, we stained the sections for Ki67, a marker for proliferating cells, and found that the number of Ki67+ RGCs was reduced upon the interference by ShCcdc85c, which was rescued by the expression of hCCDC85C or the downregulation of Numb and Numbl (Figures 7A and 7C). Therefore, these data suggest that Ccdc85c regulates progenitor proliferation through Notch signaling.

DISCUSSION

In this study, we have examined the role of Ccdc85c in regulating neural progenitor proliferation in the developing mouse neocortex. Our data suggest that Ccdc85c acts as a molecular switch that relieves the auto-inhibitory status of the polarity protein Par3, leading to its PSCP and efficient recruitment and condensation of Numb in RGCs at the VZ surface (Figure 7D). The polarized localization of Numb results in high Notch activity to maintain RGC proliferation. Disruption of the interaction between Ccdc85c and Par3 promotes the auto-inhibited conformation of Par3, which cannot recruit Numb. Freely distributed Numb attenuates Notch activity to drive RGC differentiation (Figure 7D). Thus, our data demonstrate that polarity protein Par3-mediated PSCP regulates Notch activity and thereby the proliferation of RGCs in the developing neocortex.

Apical complex proteins, including Par3, Cdc42, and Pals,[15,16,36,37] play important roles in regulating RGC proliferation and differentiation.[38] Particularly, the polarity protein Par3 is asymmetrically segregated into different daughter cells after RGC division, which allows the daughter cell to inherit a larger amount of Par3 to maintain as an RGC through higher Notch activity.[16] However, how the cell polarity bridges the Notch signaling pathway and how this connection is regulated remain unclear. Here, we present compelling evidence supporting that Ccdc85c-mediated PSCP of Par3 provides a local environment to enhance the recruitment of Notch regulator Numb to Par3 in

its open conformation and thus to control Notch activity. Our previous study showed that the open conformation of Par3 undergoes phase separation in *Drosophila* neuroblasts.[26] Here, we show that the presence of Ccdc85c in RGCs leads to the relief of the intramolecular auto-inhibition of Par3, which facilitates PSCP of Par3. Importantly, we found that the binding of Ccdc85c to Par3 promotes the recruitment of Numb to the liquid condensates (Figure 7). Disruption of the interaction between Par3 and Ccdc85c attenuates the recruitment of Numb, suggesting that Ccdc85c is important for regulating the recruitment of Numb to the Par3 condensates. It is known that Numb is an important regulator for Notch signaling.[32,39] Therefore, our data suggest that the recruitment of Numb to the Par3 condensates leads to the reduction of active Numb, which is required for the maintenance of the RGC fate. In contrast, when Ccdc85c is depleted, Par3 undergoes intramolecular inhibition, which prevents Numb from binding to Par3. Dispersed active Numb inhibits Notch signaling, which drives RGC differentiation (Figure 7D). Thus, Ccdc85c bridges the cell polarity with Notch signaling in RGCs, suggesting a dynamic mechanism via PSCP.

Phase separation has been implicated in several processes to exert diverse functions in a spatiotemporal manner.[40–43] Via intra- and/or intermolecular multivalent interactions, specific biomolecules undergo autonomous phase separation (sometimes coupled percolation) to form membrane-less organelles with unique functions.[28,29,44] During neuronal development, phase separation provides a unique assembly to recruit multiple components to control neural progenitor divisions or synaptic transmission.[26,45,46] Particularly, the Par complex undergoes phase separation at the apical membrane of the *Drosophila* neuroblast, which is important for the establishment of apical-basal polarity and the following cell fate determination of neural progenitors.[26,47] However, whether this mechanism is conserved in regulating RGC proliferation and differentiation in the developing mammalian brain remains unclear. Here, we found that polarity protein Par3-mediated PSCP is controlled by the interaction with Ccdc85c, which connects with Notch signaling to regulate RGC proliferation. Together with the observations from the *Drosophila* neuroblasts and the functions of Par3 in RGCs, we believe that phase separation may be an important way to regulate RGC proliferation and differentiation, although we could not characterize the properties of biomolecular condensates in RGCs *in vivo* due to technical difficulties. In the future, it would be interesting to examine the dynamics of biomolecular condensates mediated by polarity proteins *in vivo* to determine the daughter cell fate of RGCs.

Apical complex proteins, including polarity proteins and adhesion proteins, are important for anchoring RGCs at the apical VZ. Disruption of these proteins could lead to cortical malformation. For example, depletion of cdc42, Pals1, and Lgl1 results in the disruption of apical VZ and cortical heterotopia,[36,37,48,49] suggesting essential roles of the apical complex proteins in the maintenance of RGCs within the VZ. We found that downregulation of Ccdc85c led to the absence of RGCs from the VZ (Figure 1). However, we did not observe the disruption of the apical VZ. This is likely because we only electroporated a portion of RGCs within the VZ. It will be interesting to examine whether Ccdc85c interacts with other apical complex proteins to regulate
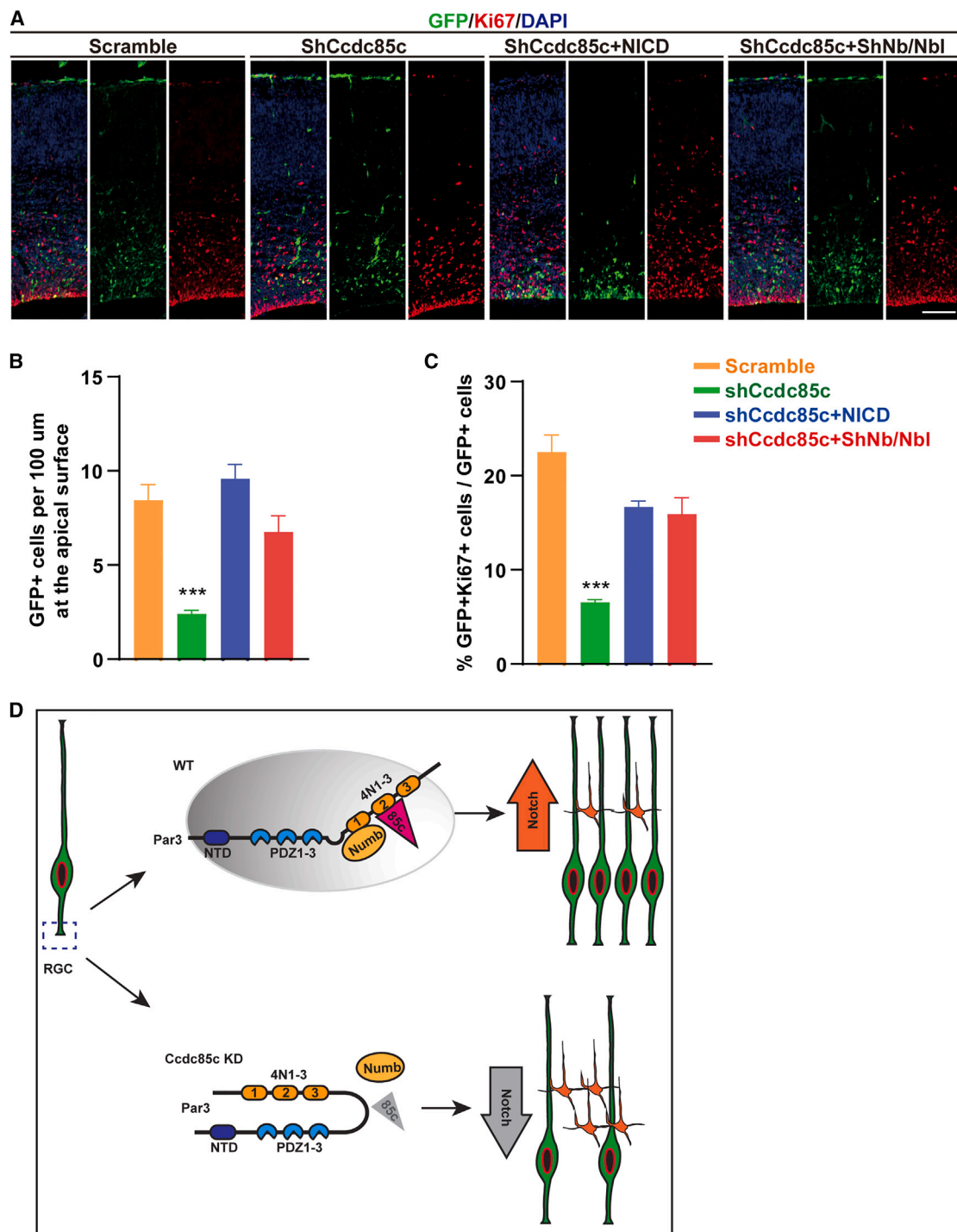
Figure 7. Ccdc85c acts through Notch signaling to regulate the maintenance of RGCs in the VZ

(A) Representative images of brain sections showing that over-expression of plasmids expressing NICD (Notch intracellular domain) or shRNAs against Numb/Numb-like (ShNb/Nbl) could rescue the deamination of RGCs from the VZ caused by the downregulation of Ccdc85c.

(B) Quantification of the number of GFP+ cells located at the VZ surface.

(C) Quantification of the percentage of proliferating cells (GFP and Ki67 double positive).

Scale bar: 50 μm. At least three brains were analyzed. Data are shown as mean ± SEM. One-way ANOVA test was used. ***p < 0.001.

(D) Working model. Ccdc85c interacts with the apical polarity protein Par3, which promotes the PSCP of Par3 and the recruitment of Numb, the Notch regulator. This, in turn, leads to the activation of Notch signaling and promotes RGC proliferation. In contrast, Par3 undergoes an auto-inhibited conformation that cannot recruit Numb. The released Numb antagonizes Notch activity, which leads to RGC differentiation.

the maintenance of RGCs within the VZ in the future. In the developing human brain, a large number of outer RGCs (oRGs) are located in the outer sub-VZ without expressing the polarity protein Par3.[3,50,51] However, these cells maintain their proliferative capacity. This suggests that apical complex proteins may play dual roles to regulate RGC proliferation and the anchoring in the VZ. It would be interesting to investigate whether Ccdc85c is involved in regulating oRG generation in human cerebral organoids.

Limitations of the study

We report in this study that polarity protein Par3-mediated PSCP is important for regulating Notch activity to control the proliferation of RGCs in the developing neocortex. The PSCP of Par3 was examined largely *in vitro* using cell lines to overcome current difficulties in studying PSCP *in vivo* directly, in particular in the developing brain. Therefore, PSCP formation *in vivo* could be potentially more complicated than *in vitro*. Using *in utero* electroporation, we provided the functional analysis, which supports our biochemistry analysis. Nevertheless, it is important to investigate PSCP formation *in vivo* with advanced techniques in the future.

Due to the lack of effective antibodies against Par3, Numb, and Ccdc85c, we examined the localization of these proteins by expression of their transcripts (Figures S3 and S5). We could not exclude the possibility that the localization of these tagged proteins is slightly different from endogenous proteins, although we tried to avoid this artifact by using low-concentration plasmids. A low level expression of Par3 has been shown to localize to the apical endfeet of RGCs as the endogenous protein.[16] The localization of Ccdc85c and Numb has been observed at the apical endfeet of RGCs.[20,32] Therefore, the localization of Par3, Numb, and Ccdc85c that we presented in this work is consistent with previous work. Nevertheless, it is important to use high-quality antibodies to examine the localization in the developing brain. In addition, given that Par3 and Numb are associated with the adherens junction,[32,52] the absence of RGCs from the VZ upon the downregulation of Ccdc85c could potentially be caused by a defective adherens junction. As electroporation can only target a small portion of RGCs of the brain, it is difficult to examine the integrity of the adherens junction in Ccdc85c knockdown RGCs. Therefore, Ccdc85c conditional knockout mice are useful for validating the importance of the localization of the polarity proteins and the brain development phenotype in the future.

STAR★METHODS

Detailed methods are provided in the online version of this paper and include the following:

- KEY RESOURCES TABLE
- RESOURCE AVAILABILITY
  - ○ Lead contact
  - ○ Materials availability
  - ○ Data and code availability
- EXPERIMENTAL MODEL AND SUBJECT DETAILS
  - ○ Animals
  - ○ Cell lines
  - ○ Microbe strains
- METHOD DETAILS
  - ○ Plasmids construction
  - ○ *In utero* electroporation
  - ○ Immunohistochemistry
  - ○ *En face* view
  - ○ Protein expression and purification
  - ○ GST pull-down assay
  - ○ Analytical gel filtration chromatography
  - ○ Isothermal titration calorimetry (ITC) measurements
  - ○ Co-immunoprecipitations and immunoblotting
  - ○ COS7 cell imaging and data analysis
  - ○ Competition assay
  - ○ FRAP assay
  - ○ FRET analysis
  - ○ Dynamic light scattering
  - ○ *In vitro* phase transition assay
- QUANTIFICATION AND STATISTICAL ANALYSIS

AUTHOR CONTRIBUTIONS

Y.X. and W.W. conceived and designed the project. J.X. performed biochemical experiments with help from Y.Z. A.G. carried out all the cell-based experiments and competition assays. X.D. and Y.C. performed the functional experiments carried out in the WT mouse model with help from Y.H. and W.Z. J.X., X.D., A.G., and Y.C. analyzed the data and prepared the figures. Y.X. wrote the manuscript with input from the other authors. W.W. and Y.X. supervised the project.

DECLARATION OF INTERESTS

The authors declare no competing interests.

INCLUSION AND DIVERSITY

We support inclusive, diverse, and equitable conduct of research.

REFERENCES

1. Lin, Y., Yang, J., Shen, Z., Ma, J., Simons, B.D., and Shi, S.H. (2021). Behavior and lineage progression of neural progenitors in the mammalian cortex. Curr. Opin. Neurobiol. *66*, 144–157. https://doi.org/10.1016/j.conb.2020.10.017.

2. Kriegstein, A., and Alvarez-Buylla, A. (2009). The glial nature of embryonic and adult neural stem cells. Annu. Rev. Neurosci. *32*, 149–184. https://doi.org/10.1146/annurev.neuro.051508.135600.

3. Lui, J.H., Hansen, D.V., and Kriegstein, A.R. (2011). Development and evolution of the human neocortex. Cell *146*, 18–36. https://doi.org/10.1016/j.cell.2011.06.030.

4. Taverna, E., Götz, M., and Huttner, W.B. (2014). The cell biology of neurogenesis: toward an understanding of the development and evolution of the neocortex. Annu. Rev. Cell Dev. Biol. *30*, 465–502. https://doi.org/10.1146/annurev-cellbio-101011-155801.

5. Götz, M., and Huttner, W.B. (2005). The cell biology of neurogenesis. Nat. Rev. Mol. Cell Biol. *6*, 777–788. https://doi.org/10.1038/nrm1739.

6. Borrell, V. (2019). Recent advances in understanding neocortical development. F1000Res *8*, F1000. https://doi.org/10.12688/f1000research.20332.1.

7. Rakic, P. (1988). Specification of cerebral cortical areas. Science *241*, 170–176. https://doi.org/10.1126/science.3291116.

8. Tang, T., Zhang, Y., Wang, Y., Cai, Z., Lu, Z., Li, L., Huang, R., Hagelkruys, A., Matthias, P., Zhang, H., et al. (2019). HDAC1 and HDAC2 regulate intermediate progenitor positioning to safeguard neocortical development. Neuron *101*, 1117–1133.e5. https://doi.org/10.1016/j.neuron.2019.01.007.

9. Klingler, E., Francis, F., Jabaudon, D., and Cappello, S. (2021). Mapping the Molecular and Cellular Complexity of Cortical Malformations. Science *371*. https://doi.org/10.1126/science.aba4517.

10. Matsuzaki, F., and Shitamukai, A. (2015). Cell division modes and cleavage planes of neural progenitors during mammalian cortical development. Cold Spring Harbor Perspect. Biol. *7*, a015719. https://doi.org/10.1101/cshperspect.a015719.

11. Delaunay, D., Kawaguchi, A., Dehay, C., and Matsuzaki, F. (2017). Division modes and physical asymmetry in cerebral cortex progenitors. Curr. Opin. Neurobiol. *42*, 75–83. https://doi.org/10.1016/j.conb.2016.11.009.

12. Fujita, I., Shitamukai, A., Kusumoto, F., Mase, S., Suetsugu, T., Omori, A., Kato, K., Abe, T., Shioi, G., Konno, D., and Matsuzaki, F. (2020). Endfoot regeneration restricts radial glial state and prevents translocation into the outer subventricular zone in early mammalian brain development. Nat. Cell Biol. *22*, 26–37. https://doi.org/10.1038/s41556-019-0436-9.

13. Kusek, G., Campbell, M., Doyle, F., Tenenbaum, S.A., Kiebler, M., and Temple, S. (2012). Asymmetric segregation of the double-stranded RNA binding protein Staufen2 during mammalian neural stem cell divisions promotes lineage progression. Cell Stem Cell *11*, 505–516. https://doi.org/10.1016/j.stem.2012.06.006.

14. Vessey, J.P., Amadei, G., Burns, S.E., Kiebler, M.A., Kaplan, D.R., and Miller, F.D. (2012). An asymmetrically localized Staufen2-dependent RNA complex regulates maintenance of mammalian neural stem cells. Cell Stem Cell *11*, 517–528. https://doi.org/10.1016/j.stem.2012.06.010.

15. Costa, M.R., Wen, G., Lepier, A., Schroeder, T., and Götz, M. (2008). Par-complex proteins promote proliferative progenitor divisions in the developing mouse cerebral cortex. Development *135*, 11–22. https://doi.org/10.1242/dev.009951.

16. Bultje, R.S., Castaneda-Castellanos, D.R., Jan, L.Y., Jan, Y.N., Kriegstein, A.R., and Shi, S.H. (2009). Mammalian Par3 regulates progenitor cell asymmetric division via notch signaling in the developing neocortex. Neuron *63*, 189–202. https://doi.org/10.1016/j.neuron.2009.07.004.

17. Knoblich, J.A. (2008). Mechanisms of asymmetric stem cell division. Cell *132*, 583–597. https://doi.org/10.1016/j.cell.2008.02.007.

18. Wirtz-Peitz, F., Nishimura, T., and Knoblich, J.A. (2008). Linking cell cycle to asymmetric division: aurora-A phosphorylates the Par complex to regulate Numb localization. Cell *135*, 161–173. https://doi.org/10.1016/j.cell.2008.07.049.

19. Marthiens, V., and ffrench-Constant, C. (2009). Adherens junction domains are split by asymmetric division of embryonic neural stem cells. EMBO Rep. *10*, 515–520. https://doi.org/10.1038/embor.2009.36.

20. Mori, N., Kuwamura, M., Tanaka, N., Hirano, R., Nabe, M., Ibuki, M., and Yamate, J. (2012). Ccdc85c encoding a protein at apical junctions of radial glia is disrupted in hemorrhagic hydrocephalus (hhy) mice. Am. J. Pathol. *180*, 314–327. https://doi.org/10.1016/j.ajpath.2011.09.014.

21. Konishi, S., Tanaka, N., Mashimo, T., Yamamoto, T., Sakuma, T., Kaneko, T., Tanaka, M., Izawa, T., Yamate, J., and Kuwamura, M. (2020). Pathological characteristics of Ccdc85c knockout rats: a rat model of genetic hydrocephalus. Exp. Anim. *69*, 26–33. https://doi.org/10.1538/expanim.19-0005.

22. Shariati, S.A.M., Lau, P., Hassan, B.A., Müller, U., Dotti, C.G., De Strooper, B., and Gärtner, A. (2013). APLP2 regulates neuronal stem cell differentiation during cortical development. J. Cell Sci. *126*, 1268–1277. https://doi.org/10.1242/jcs.122440.

23. Shin, K., Fogg, V.C., and Margolis, B. (2006). Tight junctions and cell polarity. Annu. Rev. Cell Dev. Biol. *22*, 207–235. https://doi.org/10.1146/annurev.cellbio.22.010305.104219.

24. Schmoranzer, J., Fawcett, J.P., Segura, M., Tan, S., Vallee, R.B., Pawson, T., and Gundersen, G.G. (2009). Par3 and dynein associate to regulate local microtubule dynamics and centrosome orientation during migration. Curr. Biol. *19*, 1065–1074. https://doi.org/10.1016/j.cub.2009.05.065.

25. Martin-Belmonte, F., and Mostov, K. (2008). Regulation of cell polarity during epithelial morphogenesis. Curr. Opin. Cell Biol. *20*, 227–234. https://doi.org/10.1016/j.ceb.2008.01.001.

26. Liu, Z., Yang, Y., Gu, A., Xu, J., Mao, Y., Lu, H., Hu, W., Lei, Q.Y., Li, Z., Zhang, M., et al. (2020). Par complex cluster formation mediated by phase separation. Nat. Commun. *11*, 2266. https://doi.org/10.1038/s41467-020-16135-6.

27. Kar, M., Dar, F., Welsh, T.J., Vogel, L.T., Kühnemuth, R., Majumdar, A., Krainer, G., Franzmann, T.M., Alberti, S., Seidel, C.A.M., et al. (2022). Phase-separating RNA-binding proteins form heterogeneous distributions of clusters in subsaturated solutions. Proc. Natl. Acad. Sci. USA *119*, e2202222119. https://doi.org/10.1073/pnas.2202222119.

28. Mittag, T., and Pappu, R.V. (2022). A conceptual framework for understanding phase separation and addressing open questions and challenges. Mol. Cell. *82*, 2201–2214. https://doi.org/10.1016/j.molcel.2022.05.018.

29. Deniz, A.A. (2022). Percolation physics and density transition frameworks converge in biomolecular condensation. Proc. Natl. Acad. Sci. USA *119*, e2210177119. https://doi.org/10.1073/pnas.2210177119.

30. Powers, S.K., Holehouse, A.S., Korasick, D.A., Schreiber, K.H., Clark, N.M., Jing, H., Emenecker, R., Han, S., Tycksen, E., Hwang, I., et al. (2019). Nucleo-cytoplasmic partitioning of ARF proteins controls auxin responses in Arabidopsis thaliana. Mol. Cell. *76*, 177–190.e5. https://doi.org/10.1016/j.molcel.2019.06.044.

31. Chen, S., Chen, J., Shi, H., Wei, M., Castaneda-Castellanos, D.R., Bultje, R.S., Pei, X., Kriegstein, A.R., Zhang, M., and Shi, S.H. (2013). Regulation of microtubule stability and organization by mammalian Par3 in specifying neuronal polarity. Dev. Cell *24*, 26–40. https://doi.org/10.1016/j.devcel.2012.11.014.

32. Rasin, M.R., Gazula, V.R., Breunig, J.J., Kwan, K.Y., Johnson, M.B., Liu-Chen, S., Li, H.S., Jan, L.Y., Jan, Y.N., Rakic, P., and Sestan, N. (2007). Numb and Numbl are required for maintenance of cadherin-based adhesion and polarity of neural progenitors. Nat. Neurosci. *10*, 819–827. https://doi.org/10.1038/nn1924.

33. Gaiano, N., and Fishell, G. (2002). The role of notch in promoting glial and neural stem cell fates. Annu. Rev. Neurosci. *25*, 471–490. https://doi.org/10.1146/annurev.neuro.25.030702.130823.

34. Shen, Q., Zhong, W., Jan, Y.N., and Temple, S. (2002). Asymmetric Numb distribution is critical for asymmetric cell division of mouse cerebral cortical stem cells and neuroblasts. Development *129*, 4843–4853. https://doi.org/10.1242/dev.129.20.4843.

35. Pierfelice, T., Alberi, L., and Gaiano, N. (2011). Notch in the vertebrate nervous system: an old dog with new tricks. Neuron *69*, 840–855. https://doi.org/10.1016/j.neuron.2011.02.031.

36. Cappello, S., Attardo, A., Wu, X., Iwasato, T., Itohara, S., Wilsch-Bräuninger, M., Eilken, H.M., Rieger, M.A., Schroeder, T.T., Huttner, W.B., et al. (2006). The Rho-GTPase cdc42 regulates neural progenitor fate at the apical surface. Nat. Neurosci. *9*, 1099–1107. https://doi.org/10.1038/nn1744.

37. Kim, S., Lehtinen, M.K., Sessa, A., Zappaterra, M.W., Cho, S.H., Gonzalez, D., Boggan, B., Austin, C.A., Wijnholds, J., Gambello, M.J., et al. (2010). The apical complex couples cell fate and cell survival to cerebral cortical development. Neuron *66*, 69–84. https://doi.org/10.1016/j.neuron.2010.03.019.

38. Lehtinen, M.K., and Walsh, C.A. (2011). Neurogenesis at the brain-cerebrospinal fluid interface. Annu. Rev. Cell Dev. Biol. *27*, 653–679. https://doi.org/10.1146/annurev-cellbio-092910-154026.

39. Li, H.S., Wang, D., Shen, Q., Schonemann, M.D., Gorski, J.A., Jones, K.R., Temple, S., Jan, L.Y., and Jan, Y.N. (2003). Inactivation of Numb and Numblike in embryonic dorsal forebrain impairs neurogenesis and disrupts cortical morphogenesis. Neuron *40*, 1105–1118. https://doi.org/10.1016/s0896-6273(03)00755-4.

40. Lyon, A.S., Peeples, W.B., and Rosen, M.K. (2021). A framework for understanding the functions of biomolecular condensates across scales. Nat. Rev. Mol. Cell Biol. *22*, 215–235. https://doi.org/10.1038/s41580-020-00303-z.

41. Alberti, S., and Hyman, A.A. (2021). Biomolecular condensates at the nexus of cellular stress, protein aggregation disease and ageing. Nat. Rev. Mol. Cell Biol. *22*, 196–213. https://doi.org/10.1038/s41580-020-00326-6.

42. Zhang, H., Ji, X., Li, P., Liu, C., Lou, J., Wang, Z., Wen, W., Xiao, Y., Zhang, M., and Zhu, X. (2020). Liquid-liquid phase separation in biology: mechanisms, physiological functions and human diseases. Sci. China Life Sci. *63*, 953–985. https://doi.org/10.1007/s11427-020-1702-x.

43. Shin, Y., and Brangwynne, C.P. (2017). Liquid Phase Condensation in Cell Physiology and Disease. Science (New York, N.Y.) *357*. https://doi.org/10.1126/science.aaf4382.

44. Li, P., Banjade, S., Cheng, H.C., Kim, S., Chen, B., Guo, L., Llaguno, M., Hollingsworth, J.V., King, D.S., Banani, S.F., et al. (2012). Phase transitions in the assembly of multivalent signalling proteins. Nature *483*, 336–340. https://doi.org/10.1038/nature10879.

45. Shan, Z., Tu, Y., Yang, Y., Liu, Z., Zeng, M., Xu, H., Long, J., Zhang, M., Cai, Y., and Wen, W. (2018). Basal condensation of Numb and Pon complex via phase transition during Drosophila neuroblast asymmetric division. Nat. Commun. *9*, 737. https://doi.org/10.1038/s41467-018-03077-3.

46. Wu, X., Cai, Q., Feng, Z., and Zhang, M. (2020). Liquid-liquid phase separation in neuronal development and synaptic signaling. Dev. Cell *55*, 18–29. https://doi.org/10.1016/j.devcel.2020.06.012.

47. Kono, K., Yoshiura, S., Fujita, I., Okada, Y., Shitamukai, A., Shibata, T., and Matsuzaki, F. (2019). Reconstruction of Par-dependent polarity in apolar cells reveals a dynamic process of cortical polarization. Elife *8*, e45559. https://doi.org/10.7554/eLife.45559.

48. Beattie, R., Postiglione, M.P., Burnett, L.E., Laukoter, S., Streicher, C., Pauler, F.M., Xiao, G., Klezovitch, O., Vasioukhin, V., Ghashghaei, T.H., and Hippenmeyer, S. (2017). Mosaic analysis with double markers reveals distinct sequential functions of Lgl1 in neural stem cells. Neuron *94*, 517–533.e3. https://doi.org/10.1016/j.neuron.2017.04.012.

49. Jossin, Y., Lee, M., Klezovitch, O., Kon, E., Cossard, A., Lien, W.H., Fernandez, T.E., Cooper, J.A., and Vasioukhin, V. (2017). Llgl1 connects cell polarity with cell-cell adhesion in embryonic neural stem cells. Dev. Cell *41*, 481–495.e5. https://doi.org/10.1016/j.devcel.2017.05.002.

50. Pollen, A.A., Nowakowski, T.J., Chen, J., Retallack, H., Sandoval-Espinosa, C., Nicholas, C.R., Shuga, J., Liu, S.J., Oldham, M.C., Diaz, A., et al. (2015). Molecular identity of human outer radial glia during cortical development. Cell *163*, 55–67. https://doi.org/10.1016/j.cell.2015.09.004.

51. Ostrem, B., Di Lullo, E., and Kriegstein, A. (2017). oRGs and mitotic somal translocation - a role in development and disease. Curr. Opin. Neurobiol. *42*, 61–67. https://doi.org/10.1016/j.conb.2016.11.007.

52. Tepass, U. (2012). The apical polarity protein network in Drosophila epithelial cells: regulation of polarity, junctions, morphogenesis, cell growth, and survival. Annu. Rev. Cell Dev. Biol. *28*, 655–685. https://doi.org/10.1146/annurev-cellbio-092910-154033.

STAR★METHODS

KEY RESOURCES TABLE

REAGENT or RESOURCE	SOURCE	IDENTIFIER
Antibodies		
Rabbit polyclonal anti-Cux1/CDP	Santa Cruz	Cat# sc-13024; RRID: AB_2261231
Rat monoclonal [25B6] anti-Ctip2	Abcam	Cat# ab18465; RRID: AB_2064130
Chicken polyclonal anti-GFP	Aves Labs	Cat# GFP-1020; RRID: AB_10000240
Chicken polyclonal anti-GFP	Abcam	Cat# ab13970; RRID: AB_300798
Rabbit polyclonal anti-Ki67	Abcam	Cat# ab15580; RRID: AB_443209
Mouse polyclonal anti-Pax6	MBL International	Cat# PD022; RRID: AB_1520876
Rabbit polyclonal anti-Tbr2	Abcam	Cat# ab23345; RRID: AB_778267
Goat polyclonal anti-mCherry	SICGEN	Cat# AB0081; RRID: AB_2333095
Mouse monoclonal anti-DDDDK-Tag	ABclonal	Cat# AE005; RRID: AB_2770401
Mouse monoclonal anti-His-Tag	ABclonal	Cat# AE003; RRID: AB_2728734
Mouse monoclonal anti-Myc-Tag	ABclonal	Cat# AE010; RRID: AB_2770408
HRP Goat Anti-Mouse IgG	ABclonal	Cat# AS003; RRID: AB_2769851
Alexa Fluor 488 AffiniPure Donkey Anti-Chicken IgY (IgG)	Jackson ImmunoResearch Labs	Cat# 703-545-155; RRID: AB_2340375
Alexa Fluor 647-AffiniPure Donkey Anti-Rabbit IgG (H + L)	Jackson ImmunoResearch Labs	Cat# 711-605-152; RRID: AB_2492288
Alexa Fluor 647 Donkey anti-Mouse	Jackson ImmunoResearch Labs	Cat# 715-605-151; RRID: AB_2340863
Alexa Fluor 647-AffiniPure Donkey Anti-Rat IgG (H+L)	Jackson ImmunoResearch Labs	Cat# 712-605-153; RRID: AB_2340694
Donkey anti-Goat IgG (H+L) Cross-Adsorbed Secondary Antibody, Alexa Fluor™ 568	Thermo Fisher Scientific	Cat# A-11057; RRID: AB_2534104
Goat anti-Rabbit IgG (H+L) Highly Cross-Adsorbed Secondary Antibody, Alexa Fluor™ 568	Thermo Fisher Scientific	Cat# A-11036; RRID: AB_10563566
Bacterial and virus strains		
Escherichia coli BL21 (DE3) host cells	(Shan et al., 2018)[45]	N/A
Escherichia coli Rosetta host cells	(Shan et al., 2018)[45]	N/A
Chemicals, peptides, and recombinant proteins		
O.C.T.	Sakura	Cat#4583
Click-iT™ EdU Alexa Fluor™ 647 Imaging Kit	Thermo Fisher Scientific	Cat#C10340
Anti-Flag M2 affinity gel	Sigma	Cat#A2220
Protease inhibitor cocktail	Thermo Fisher Scientific	Cat#A32955
Glutathione Sepharose 4 Fast Flow,25mL	GE healthcare	Cat#17-5132-01
Ni Sepharose 6 Fast Flow,25mL	GE healthcare	Cat#17-5318-01
Phanta Super-Fidelity DNA Polymerase	Vazyme	Cat#P501-d1
T4 DNA ligase	TAKARA	Cat#2011B(Ax5)
Phenylmethanesulfonyl fluoride	Aladin	Cat#P105539-100g
DNA DL2000 Marker	Takara	Cat#3427A
NiSO$_4$	Sinopharm	Cat#10014418
Coomassie brilliant blue R-250	Sangon Biotech	Cat#A100472-0025
EDTA disodium salt dihydrate	BBI	Cat#A610185-0500
Sodium dodecyl sulfate	Sinopharm	Cat#30166428
QuickCut™	TAKARA	NA
IPTG	INALCO	Cat#1758-1400
Tryptone	Oxoid	Cat#LP0042

Continued		
REAGENT or RESOURCE	SOURCE	IDENTIFIER
Yeast Extract Powder	Oxoid	Cat#LP0021
Acrylamide	Sigma	Cat#A3553
Experimental models: Cell lines		
HEK293	ATCC	Cat# PTA-4488; RRID: CVCL_0045
COS7	ATCC	Cat# CRL-1651; RRID: CVCL_0224
Oligonucleotides		
Ccdc85c shRNA forward sequence: GA TCCCCAACCTTGACCGGCAACTTCAAT TCAAGAGATTGAAGTTGCCGGTCAAGG TTTTTTTA	This paper	N/A
Ccdc85c shRNA reverse sequence: AG CTTAAAAAAACCTTGACCGGCAACAA CTTCAATCTCTTGAATTGAAGTTGCC GGTCAAGGTTGGG	This paper	N/A
Numb shRNA target sequence: GCCGAAAGAGAGGAGATCA	(Mladen et al., 2007)[32]	N/A
Numbl shRNA target sequence: GGCACCATGAACAAGTTAC	(Mladen et al., 2007)[32]	N/A
See Table S1 for primers for Par3/Ccdc85c fragments	This paper	N/A
Recombinant DNA		
pCAGEN	Addgene	Cat#11160
pSuper	OligoEngine	Cat#VEC-PBS-0002
pCAG-GFP	Addgene	Cat#11150
pEGFP-C3	(Shan et al., 2018)[45]	N/A
pmCherry-C1	(Shan et al., 2018)[45]	N/A
pMAL-c2x	(Shan et al., 2018)[45]	N/A
pET32a	(Shan et al., 2018)[45]	N/A
Software and algorithms		
Image J	NIH	https://imagej.nih.gov/ij/; RRID: SCR_003070
NIS Element version 5.11	Nikon	https://www.microscope.healthcare.nikon.com/products/software; RRID:SCR_014329
GraphPad Prism	GraphPad Software	https://www.graphpad.com/; RRID:SCR_002798
Adobe Photoshop	Adobe	https://www.adobe.com/products/photoshop.html; RRID:SCR_014199
Adobe Illustrator	Adobe	http://www.adobe.com/products/illustrato.html; RRID:SCR_010279

RESOURCE AVAILABILITY

Lead contact
Further information and requests for resources and reagents should be directed to and will be fulfilled by the Lead Contact Yunli Xie (yunli.xie@fudan.edu.cn).

Materials availability
This study did not generate new unique reagents.

Data and code availability
- All data reported in this paper will be shared by the lead contact upon request.
- This paper does not report original code.
- Any additional information required to reanalyze the data reported in this paper is available from the lead contact upon request.

EXPERIMENTAL MODEL AND SUBJECT DETAILS

Animals

C57BL/6J mice were used in this paper. The day of vaginal plug detection was designated as embryonic day 0.5 (E0.5), and the day of birth was referred to as postnatal day 0 (P0). E14.5 embryos were used for *in utero* electroporation and analyzed 3 days later or after birth. Both male and female littermates were randomly assigned to experimental groups for all experiments. All animal work was approved by Animal Care and Use Committee of Shanghai Medical College of Fudan University

Cell lines

Human HEK293 cells and COS7 cells (from American Type Culture Collection (ATCC)) were grown in Dulbecco's modified Eagle medium (Gibco, Cat#11995065) containing 10% fetal bovine serum (Gibco, Cat#10099141) in an incubator with 5% CO_2 at 37°C. Cells were transiently co-transfected using polyethylenimine transfection reagent (Polysciences). Cells were harvested 36 h post transfection

Microbe strains

Escherichia coli BL21 (DE3) or Rosetta host cells were cultured on a shaker at 37°C with a speed of 220 rpm for 12-16 hours. Once the OD600 absorbance value reached 0.6-0.8, indicating optimal bacterial growth in the logarithmic phase, the bacterial solution was cooled for 0.5-1 hour in a 4°C refrigerator. The IPTG was then added with a final concentration of 0.3 mM when the temperature of the medium reached around 16°C to induce protein expression. Subsequently, cells were exposed to induction for 16-18 hours at 220 rpm, 16°C. It is worth noting that *Escherichia coli* reproduces asexually.

METHOD DETAILS

Plasmids construction

Human CCDC85C cDNA was cloned into pCAGEN vector. Point mutations were made by the site-directed mutagenesis and confirmed by Sanger sequencing. GFP-Par3 was cloned into Sal I/Not I sites of the pEGFP-C3 vector. mCherry-Ccdc85c and mCherry-Numb were cloned into EcoR I/Sal I sites of the pmCherry-C1 vector. For RNA interference, the shRNA oligos against Ccdc85c, Numb, and Numbl were cloned into the pSuper vector. The Numb/Nubml shRNA oligo sequences were refer to Mladen-Roko et al.[32] The primer sequences are listed in Table S1.

In utero electroporation

The *in utero* electroporation (IUE) procedure followed a protocol previously described by Tang et al.[8] Briefly, pregnant mice (E14.5) were anaesthetized and the uterine horns were exposed.

The desired plasmids (1.5-3 μg/μL) were injected into the lateral ventricles of the embryos. Electroporation was performed using a BTX electroporation system (ECM830) with five 50ms pulses of 34V, applied at 950ms intervals which were dependent on the embryonic age. The uterine horns were carefully repositioned back into the abdominal cavity and the wound was sutured. Embryos were analyzed 3 days later or at P7.

Immunohistochemistry

The embryonic brains were fixed with 4% PFA overnight at 4°C, followed by transferring into 30% sucrose in PBS for 24h at least. The brains were then embedded in O.C.T compound (Sakura, Cat#4583) and sectioned at 14 μm thickness for embryonic brain analysi and 30 μm thickness for postnatal brain analysis. For immunostaining, brain sections were permeabilized with 0.5% Triton X-100 for 30 mins at room temperature. The sections were then blocked with a combination of 0.5% Triton X-100, 5% normal goat serum in PBS at room temperature for 1 hour before being incubated overnight at 4°C with the relevant primary antibody. Following washing with PBS, the sections were then treated with suitable secondary antibodies for 2 hours at room temperature in the dark, before mounting for analysis. A comprehensive list of all the details of the antibodies used in the study is available in the key resources table.

En face view

For the *en face* view, E13.5 embryos were subjected to IUE and analyzed after 24h. The brain was carefully separated from the embryo and placed in a culture dish filled with cold 1X PBS on ice. The cortex was then removed carefully under a stereomicroscope and transferred to a centrifuge tube containing 4% PFA for overnight incubation at 4°C. The brain was then washed with 1X PBS thoroughly. Next, permeabilization with 0.5% Triton X-100 for 1 hour at room temperature was performed. After blocking with the blocking buffer (0.5% Triton X-100, 5% normal goat serum in PBS) for 1h at room temperature, the sections were then incubated with the desired primary antibody for 2 days at 4°C. After washing with PBS, appropriate secondary antibodies were then incubated for 2h at room temperature in the dark. Finally, the cortex was carefully transferred to the slide to unfold and flatten, ensuring that the surface of the ventricle was facing upward. After slightly drying the excess liquid, the cortex was mounted before analysis.

Protein expression and purification

The human Par3 fragments (Uniprot ID: Q8TEW0-11) and the human CCDC85C fragments (Uniprot ID: A6NKD9s) were individually cloned into pMAL-c2x or a modified version of pET32a vector.[45] Mutations were generated utilizing the standard PCR-based mutagenesis method and confirmed via DNA sequencing. The recombinant proteins were expressed in *Escherichia coli* BL21 (DE3) or Rosetta host cells in LB medium at 16 °C. The proteins were then purified with a Ni^{2+}-NTA agarose affinity column, followed by size-exclusion chromatography (using HiLoad 26/600 superdex 200 pg columns on an AKTA FPLC system, GE Healthcare) using buffer A, which contains 50 mM Tris (pH 8.0), 100 mM NaCl, 1mM β-ME, and 1 mM EDTA.

GST pull-down assay

For the GST pull-down assay, 4 nmoL of GST fusion proteins were loaded onto 40 μL GSH-Sepharose 4B slurry beads, and indicated proteinsproteins (12 nmoL) were then incubated with them in 500 μL buffer A at 4°C for 1 hour. After three washes with the same buffer, the captured proteins were eluted by boiling with SDS-loading buffer, resolved by 12% SDS-polyacrylamide gel electrophoresis (SDS-PAGE), and detected via coomassie blue staining.

Analytical gel filtration chromatography

Analytical gel filtration chromatography was performed on an AKTA Fast Protein Liquid Chromatography (FPLC) system (GE Healthcare). Protein samples were pre-concentrated to indicated concentrations and loaded onto a Superdex™ 200 increase 10/300 GL column (GE Healthcare) pre-equilibrated with the buffer A.

Isothermal titration calorimetry (ITC) measurements

The ITC measurement was conducted at 25°C using a PEAQ-ITC (MicroCal). All protein samples were dissolved in buffer A, and titrations were performed by injecting 40 μL aliquots of Ccdc85c (50-160) (0.5 mM) into Par3 (1070-1217) (0.04 mM) at 2 minutes time intervals. The titration data were analyzed using the Malvern MicroCal PEAQ-ITC analysis program. The Kd error represents the fitted error obtained from the data analysis software when using the one-site binding model to fit the ITC data.

Co-immunoprecipitations and immunoblotting

HEK293T cells were co-transfected with the full-length human CCDC85C and human Par3 using polyethylenimine transfection reagent (Poly-sciences). Cells were harvested 36h post-transfection and lysed in the lysis buffer consisting of 50 mM Tris (pH 7.4), 150 mM NaCl, 1% Nonidet P-40 and protease inhibitor cocktail (Thermo Fisher, A32955). Each lysate was then incubated with anti-Flag M2 affinity gel (Sigma, Cat#A2220) for 4h. After extensive wash with the lysis buffer, the above proteins captured by affinity beads were used for immunoblotting.

The captured proteins were boiled in SDS-PAGE loading buffer and separated by SDS-PAGE. The proteins were transferred onto a 0.45 μm polyvinylidene difluoride (PVDF) membrane (Millipore). Subsequently, the membrane was blocked using 5% bovine serum albumin in TBST buffer (20 mM Tris-HCl (pH 7.4), 137 mM NaCl, and 0.1% Tween-20) at room temperature for 1h. This was followed by incubation with primary antibodies at a 1/2000 dilution at 4 °C overnight. Membranes were washed three times with TBST buffer, incubated with HRP goat anti-mouse antibody (ABclonal, AS003), and visualized on a LAS4000 Chemiluminescence Imaging System. Antibodies are listed in key resources table.

COS7 cell imaging and data analysis

Par3 and Ccdc85c plasmids were individually or co-transfected into COS7 cells, utilizing polyethylenimine transfection reagent (Poly-sciences). Cells were fixed with 4% paraformaldehyde and mounted onto glass slides for imaging using an OLYMPUS confocal microscope by a 60X oil immersion lens with DAPI staining. Puncta-counting assay data were collected from 3-6 independent batches of cultures as indicated in the figure. In each batch, at least 600 fluorescence-positive cells were counted for each group of experiments. A cell with more than two visible fluorescence puncta was considered a puncta-positive cell. All experiments were conducted in a blinded fashion.

Competition assay

Mouse Numb and human Par3 plasmid were co-transfected into HEK293T cells (from ATCC) using PEI (Poly-sciences) as the transfection reagent. Cells were harvested 36h post transfection and lysed in lysis buffer. Each lysate was incubated with anti-Flag M2 affinity gel (Sigma, Cat#A2220) for 2h. Next, the lysate was incubated for 1h in the presence of 0, 1, or 4 nmoL of purified MBP-His-Ccdc85c (50-160). After washing three times, proteins captured by affinity beads were eluted by boiling and subjected to immunoblotting.

FRAP assay

COS7 cells were cultured in glass-bottom dishes and transfected. At 36 hours post-transfection, the FRAP assay was performed using a Leica TCS SP8 confocal microscope. Puncta with diameters approximately 2.0 μm were analyzed. The GFP signal was bleached using a 488-nm laser beam. The fluorescence intensity difference between pre-bleaching and time 0 (immediately following the photo-bleaching pulse) was then normalized to 100%. The fluorescence intensity of similar puncta/cytoplasm regions without photo-bleaching was used as internal reference.

FRET analysis

COS7 cells cultured in glass-bottom dishes were mounted for acquiring FRET images at 36 hours post-transfection. FRET images were captured utilizing a Leica TCS SP8 confocal microscope. In order to photobleach YFP, the cells were illuminated until 20% of the original fluorescence intensity was detected. Under these conditions, CFP direct bleaching was minimized. The increase in CFP emission under CFP excitation after photobleaching YFP indicated FRET. The FRET efficiency of each cell, represented as FRETeff (%), was calculated as (CFPpost- CFPpre)/CFPpost.

Dynamic light scattering

Dynamic light scattering measurements of Par3N were conducted at 25°C using a DynaPro Plate Reader (WYATT) with 158° forward scattering. The measurements were recorded for 10 seconds using a DYNAMICS V7 (WYATT) to obtain autocorrelations. Each experiment was repeated at least three times. The hydrodynamic radius estimates were analyzed using the DYNAMICS V7 (WYATT) software. Par3N was tested in a solution containing 50 mM Tris (pH 8.0), 100 mM NaCl, 1mM b-ME, and 1 mM EDTA.

In vitro phase transition assay

For fluorescence assay, Par3N was purified in buffer containing 100 mM $NaHCO_3$ (pH 8.3), 300 mM NaCl, 1 mM EDTA, and 1 mM DTT. iFluorTM 488 NHS ester was incubated with Par3N at room temperature for 1h, with the fluorophore to protein molar ratio maintained at 1:1. The reaction was quenched using 200 mM Tris (pH 8.0), and the chemically labeled proteins were further purified into buffer A using a Hitrap desalting column. The iFluorTM 488-labeled Par3N mixed with 50 molar ratios of unlabeled Par3N at varying concentrations was observed in a flow chamber at room temperature using an Olympus IX73 fluorescence microscope. For imaging, Par3N was injected into a homemade flow chamber comprised of a glass slide sandwiched by a coverslip with one layer of double-sided tape as a spacer for fluorescent imaging on the Olympus IX73.

QUANTIFICATION AND STATISTICAL ANALYSIS

The Nikon A1R confocal microscope (Nikon) was used to capture images. Image processing was carried out using NIS Element version 5.11 (Nikon) or Adobe Photoshop. GraphPad Prism 8 was used for statistical analysis. A two-tailed Student's t-test was used to compare two groups of data, and one-way ANOVA was used for more than two groups. All experiments were independently performed using at least 3 brains. Data were presented as mean ± SEM. $p<0.05$ was considered as significant. Significance is marked as *, $p < 0.05$; **, $p < 0.01$; ***, $p < 0.001$ and ****, $p < 0.0001$.

GraphPad Prism 8 software was used for other statistical analysis. Statistical tests and sample sizes are indicated in the figure legends. A p value of <0.05 was considered statistically significant and a p value of >0.05 was considered statistically non-significant (ns). Significance is marked as *, $p < 0.05$; **, $p < 0.01$; ***, $p < 0.001$ and ****, $p < 0.0001$.